Journal of Molecular Structure 980 (2010) 51–58

Contents lists available at ScienceDirect

Journal of Molecular Structure

journal homepage: www.elsevier.com/locate/molstruc

Hydrogen bonding and thermodynamic properties of (*R*,*S*)- and (*R*)-alanine-based selector

Ivana Gazić Smilović, Krešimir Molčanov, Vladimir Vinković, Biserka Kojić-Prodić, Andreja Lesac *

Ruđer Bošković Institute, P.O. Box 180, Bijenička cesta 54, HR-10002 Zagreb, Croatia

ARTICLE INFO

Article history:
Received 1 April 2010
Received in revised form 29 June 2010
Accepted 29 June 2010
Available online 6 July 2010

Keywords:
(*R*,*S*)-, (*R*)- and (*S*)-alanine-based compounds
X-ray structure
Thermal behavior
Hydrogen bonding
Conformational disorder

ABSTRACT

We report on structural investigation of homochiral and heterochiral alanine-based selector 4-butylamino-*N*-[1-(3,5-dimethyl-phenylcarbamoyl)-ethyl]-3,5-dinitrobenzamide (**I**) preformed by X-ray structure analysis and thermo-optical analysis. The topologies of hydrogen bonding of racemate crystals and the homochiral crystals are significantly different and affect their thermodynamic stabilities. The heterochiral ***rac*-I** crystal is characterized by high temperature and entropy fusion due to the compact packing of the molecules of opposite chirality (hydrogen bonded *RS* pairs). On the contrary, packing of homochiral molecules is less compact and crystals reveal low thermodynamic stability related to conformational flexibility.

1. Introduction

Substituted dihydropyrimidinones (DHPMs) are known to exhibit a wide range of biological activities such as antiviral, antitumor, antibacterial, and anti-inflammatory properties, including Ca^{2+} channel openers [1,2]. As for many other drugs, the biological activity of most of the DHPMs strongly depends on their absolute stereochemistry. Pharmacologic studies with resolved enantiomers have demonstrated multiple differences in potency or even that the desired effect resides in one enantiomer, solely [2,3]. Therefore, homochiral precursors and final products are of outmost importance in pharmaceutical industry [4].

In the frame of our research on brush-type chiral stationary phases (CSPs) we developed a group of chiral selectors based on (*S*)-alanine and 4-chloro-3,5-dinitrobenzoic acid which proved to be efficient for the liquid chromatography resolution of several racemic dihydropyrimidonic compounds [5,6]. Molecular recognition of DHPM by a chiral selector depends on the molecular geometry and accessible conformations of the chiral selector itself. Investigations of the crystal structures of an enantiomer and its corresponding racemate offer a unique opportunity to study interactions of the same molecule in different crystalline environments. Thus, homochiral interactions are those between molecules of the same chirality found in crystals of an enantiomer, whereas in the racemic compound interactions between molecules of the same and opposite chirality are heterochiral. The differences in melting entropy and enthalpy between the racemic compound and its enantiomer provide the thermodynamic background that combined with an analysis of intermolecular interactions in the crystals, can give valuable insight into the crystal stability.

For the purpose of this study the compound of general formulae **I** (Fig. 1) was selected. The structure of the compound **I** comprises dinitrobenzoyl (DNB) and dimethylphenylamide (DMA) units that are connected *via* alanine moiety. The DNB unit is primarily involved in complexation with analyte by hydrogen bonding whereas DMA defines the wall of the chiral cavity and strengthen the rigidity of the chiral selector, allowing uniform approach of analyte [7]. In addition, presence of aminobutyl moiety at DMB unit that replaces the spacer towards the silica, might contribute to conformational flexibility and facilitate preorganization of the chiral selector in such a way that interaction points are moved away from the silica surface [6].

In the present work, selectors ***rac*-I** and both enantiomers denoted as ***S*-I** and ***R*-I**, have been prepared from corresponding racemic, (*S*)-alanine and non-natural (*R*)-alanine, respectively and their conformational features studied by X-ray diffraction and thermo-optical methods; hot-stage polarizing optical microscopy (HS-POM) and differential scanning calorimetry (DSC).

2. Experimental

2.1. General – synthesis of the selectors

Thin layer chromatography was performed on DC-Alufolien Kieselgel 60 F_{254} (Merck) and the compounds were detected using

* Corresponding author. Tel.: +385 1 4571 300; fax: +385 1 4680 108.
E-mail address: andreja.lesac@irb.hr (A. Lesac).

0022-2860/$ - see front matter © 2010 Elsevier B.V. All rights reserved.
doi:10.1016/j.molstruc.2010.06.036

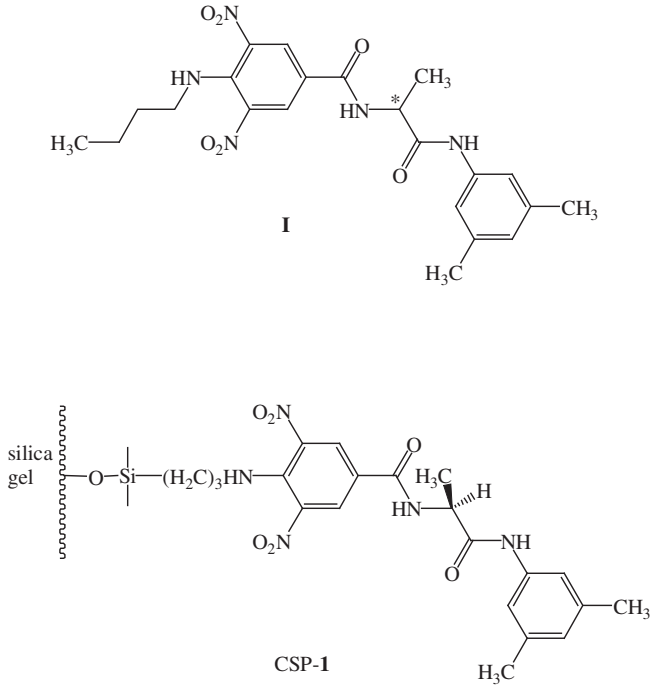

Fig. 1. General chemical diagram of the alanine-based chiral selector **I** and schematic presentation of the chiral stationary phase CSP-**1** and its soluble analogue ***S*-I**.

Spectroline UV lamp at 254 nm. Column chromatography was performed by using silica gel, particle size 0.063–0.200 mm (J.T. Baker). ^{1}H NMR and ^{13}C NMR spectra were recorded on Bruker AV 300 spectrometer. The melting points were determined using an Olympus BX51 polarizing microscope equipped with a Linkam TH600 hot stage and PR600 temperature controller. Optical rotations were measured using the Optical Activity AA-10 automatic polarimeter.

Suspension of 4-chloro-*N*-[1-(3,5-dimethyl-phenylcarbamoyl)-ethyl]-3,5-dinitrobenzamide [5] of appropriate configuration (0.5 mmol), *n*-butylamine (1.5 mmol), previously dried overnight under solid KOH, and anhydrous tetrahydrofurane (10 mL) was stirred overnight at room temperature. Soluble chiral selectors ***R*-I** and ***S*-I** were isolated upon evaporation of the reaction mixture and chromatography on silica gel, using a mixture of solvents CH_2Cl_2/CH_3OH (10/0.5, $R_f = 0.8$) as eluent while precipitated ***rac*-I** selector was separated on G-4 filter and washed with THF. After drying in vacuum desiccator for 5 h, the pure products were obtained as the orange powders. The NMR data are identical for all three samples.

^{1}H NMR (DMSO-d_6) δ/ppm: 0.86 (3H, t, $J = 7.5$ Hz), 1.29 (2H, dt, $J = 7.5$ and 6.4 Hz), 1.41 (3H, d, $J = 7.0$ Hz), 1.58–1.63 (2H, m), 2.22 (6H, s), 2.92–3.07 (2H, m), 4.57 (1H, q, $J = 7.0$ Hz), 6.69 (1H, s), 7.23 (2H, s), 8.41 (1H, s), 8.83 (2H, s), 8.96 (1H, d, $J = 7.0$ Hz), 9.88 (1H, s). ^{13}C NMR (DMSO-d_6) δ/ppm: 13.43, 17.64, 19.26, 21.05, 30.98, 45.87, 50.13, 117.09, 119.18, 124.78, 131.04, 137.00, 137.59, 138.80, 140.51, 162.56, 171.03.

Selector ***rac*-I**; m.p.: 517 K; (*R,S*); Anal. Calcd. for $C_{22}H_{27}N_5O_6$ (457.486): C, 57.76; N, 15.31; H, 5.95%. Found: C, 57.80; N, 15.19; H, 6.08%.

Selector ***R*-I**; m.p.: 471 K; $[\alpha]_D^{20}$ (R) = −103.0 (10 mg/mL, DMF). Anal. Calcd. for $C_{22}H_{27}N_5O_6$ (457.486): C, 57.76; N, 15.31; H, 5.95%. Found: C, 57.93; N, 15.33; H, 6.07%.

Selector ***S*-I**; m.p.: 471 K; $[\alpha]_D^{20}$ (S) = +113.0 (10 mg/mL, DMF). Anal. Calcd. for $C_{22}H_{27}N_5O_6$ (457.486): C, 57.76; N, 15.31; H, 5.95%. Found: C, 58.02; N, 15.37; H, 6.09%.

2.2. X-ray structure analysis

The crystallographic analysis was carried out for ***rac*-I** and ***R*-I**, while all attempts to obtain a good crystal of ***S*-I** failed. Crystals for X-ray diffraction were obtained by slow evaporation of dimethylformamide solutions of ***rac*-I** and from dichloromethane solutions of ***R*-I**. Data collections were performed on an Enraf–Nonius CAD4 diffractometer, using a graphite monochromated Cu Kα (1.54179 Å) radiation at room temperature (RT, 293 K). The WinGX standard procedure was applied for data reduction [8]. Three standard reflections were measured every 120 min as intensity control. Absorption correction based on eight Ψ-scan reflections was performed [9] for structures ***rac*-I** and ***R*-I** (293 K). No absorption correction was performed for ***R*-I** (100 K). The structures were solved with SHELXS97 and refined with SHELXL97 [10,11]. The models were refined using the full matrix least squares refinement. Hydrogen atoms were located from a difference Fourier map and were refined as mixed free and riding entities. The atomic scattering factors were those included in SHELXL97. Molecular geometry calculations were performed with PLATON [12], and molecular graphics were prepared using ORTEP-3 [13], and CCDC-Mercury [14].

Reduced crystal quality, probably originated from conformational flexibility, of the molecules affecting the intensity data. In ***rac*-I** and molecule **B** of ***R*-I** (293 K) the displacement parameters of the atoms of butyl and nitro groups were significantly larger than those of the rest of the molecule. In molecule **A** of ***R*-I** (293 K), however, thermal motion produced unrealistic geometry of the C–C bonds and elongated, stick-shaped, ellipsoids of *n*-butyl group. Therefore, in the molecule **A** of ***R*-I** (293 K) *n*-butyl group was restrained (C–C bond length of 1.5 Å). The structure involves dynamic disorder, which could not be modeled and the high residual electron density occurred. Cooling of a crystal of ***R*-I** to 100 K reduced thermal motion of the atoms, but did not improve the quality of the data due to the increased mosaic spread. The refinement resulted in a relatively high R value and residual electron density (Table 1).

2.3. Thermal behavior

Thermal behavior was studied by two complementary techniques; hot-stage polarizing optical microscopy (HS-POM) using an Olympus BX51 polarizing microscope equipped with a Linkam TH600 hot stage and PR600 temperature controller and differential scanning calorimetry. Thermograms were recorded on Perkin-Elmer Diamond DSC, operated at scanning rates of 2–10 K min^{-1}.

3. Results and discussion

The pure enantiomers *R*- and *S*- of a compound react differently with other chiral molecules but not with other achiral molecules [15]. Enantiomers show different reaction rates with other chiral molecules (e.g. enantioselectivity of enzymes on different enantiomers) [16] and different solution behavior in pure chiral solvents [15]. As expected, for ***R*-I** and ***S*-I** enantiomers identical solubility in the achiral solvents was observed. On the other hand, whereas ***R*-I** and ***S*-I** are readily soluble in different organic solvents, e.g. ethanol, methanol, acetone, chloroform etc., ***rac*-I** is only slightly soluble in dimethylsulfoxide and hot dimethylformamide. The solubility of racemate is usually lower than that of pure enantiomers [17]. This could be an indication that the crystal structure of ***rac*-I** is much more stable than that of the optically pure **I**. Generally, the crystal packing interactions are better optimized in heterochiral (racemates) than in homochiral crystals (enantiomers) leading to higher density of racemate than of enantiomeric crystals [17,18] although the exceptions were encountered [19,20]. As a

Table 1
X-ray crystallographic data and structure refinement data for the compounds ***rac*-I**, *R*-**I** (100 K) and ***R*-I** (RT).

Compound	***rac*-I** (RT)	***R*-I** (RT)	***R*-I** (100 K)
Empirical formula	$C_{22}H_{27}N_5O_6$	$C_{22}H_{27}N_5O_6$	$C_{22}H_{27}N_5O_6$
Formula wt. (g mol^{-1})	457.49	457.49	457.49
T (K)	293	293	100
Crystal dimensions (mm)	0.25 × 0.20 × 0.10	0.32 × 0.26 × 0.12	0.40 × 0.30 × 0.10
Space group	$P-1$	$P1$	$P1$
a (Å)	8.0181(9)	7.0890(6)	6.8906(8)
b (Å)	10.5113(9)	7.9496(5)	7.8604(17)
c (Å)	14.405(2)	20.8571(13)	20.768(4)
α (°)	75.441(10)	89.211(5)	82.544(16)
β (°)	80.807(11)	89.838(6)	82.555(13)
γ (°)	73.472(8)	81.018(6)	82.377(14)
Z	2	2	2
V (Å^3)	1121.5(2)	1160.87(14)	1098.2(3)
D_{calc} (g cm^{-3})	1.355	1.309	1.383
μ (mm^{-1})	0.835	0.807	0.853
T_{min}, T_{max}	0.7916, 0.9183	–	–
Θ range (°)	3.18–76.16	2.12–76.38	2.16–76.26
Range of h, k, l	$0 < h < 10$; $-12 < k < 13$; $-17 < l < 18$	$0 < h < 8$; $-9 < k < 10$; $-26 < l < 26$	$-8 < h < 8$; $-9 < k < 0$; $-26 < l < 25$
Reflections collected	5021	5247	4932
Independent reflections	4673	4842	4932
Observed reflections ($I \geqslant 2\sigma$)	3217	4394	4731
R_{int}	0.0495	0.0500	0
R (F^2)	0.0619	0.0670	0.0706
R_w (F^2)	0.1872	0.1949	0.2009
Goodness of fit	1.022	1.001	1.015
No. of parameters	383	644	620
No. of restraints	0	26	3
$\Delta\rho_{max}$, $\Delta\rho_{min}$ (eÅ^{-3})	0.32; −0.29	0.56; −0.33	0.61; −0.60

consequence heterochiral crystals display greater stability and higher melting points than homochiral crystals [18–21]. The structural studies involving investigation on various temperatures (X-ray, microscopy, DSC) were performed in order to gather valuable information on the molecular geometry, accessible conformations of the compound **I** and their thermodynamic stability. The difference in molecular geometry and crystal packing between heterochiral and homochiral crystals in conjunction with their thermodynamic behavior will be discussed accordingly.

3.1. Molecular structures of *rac*-I and *R*-I

Single crystal X-ray structure of *R*-**I** was measured at room and low temperature (100 K, Table 1) whereas ***rac*-I** was measured at room temperature, only, to avoid considerable mosaicity spread. The heterochiral crystals reveal the triclinic centrosymmetric space group with a single molecule in an asymmetric unit (Fig. 2, Table 1) whereas homochiral crystals appear in the analogous noncentrosymmetric space group with two molecules in the asymmetric unit, **A** and **B** that differ in torsional angles of the alanine moiety (Fig. 3, Table 2).

The homochiral crystals measured at room- and low-temperatures exhibit two different conformations (Fig. 3a and b, Table 2). The conformational differences are primarily induced by flexibility of *n*-butyl chain but also different orientations of nitro groups. The conformation of *n*-butyl chain in ***R*-I** (molecules **A** and **B**) at RT is *antiperiplanar* about C2–C3 and C3–C4 bonds, whereas in the low-temperature conformers it is (±)*gauche* [22]. The former conformation of *n*-butyl chain was also found in ***rac*-I** (RT).

Comparison of dihedral angles between least-squares best planes of aromatic rings C5 → C10 and C15 → C20 illustrate the conformational difference of the environment around the stereogenic centres (C12) in homochiral and heterochiral molecules at RT (Fig. 4). Thus, the values for dihedral angles in homochiral molecules **A** and **B** amount 16.6° and 8.1°, respectively, while in heterochiral ***rac*-I** it reaches 25.5°. The coplanarity of the N5 amide bond with the aromatic ring C15 → C20 contributes to more compact packing in ***rac*-I** than in ***R*-I** in which this bond deviates (in both

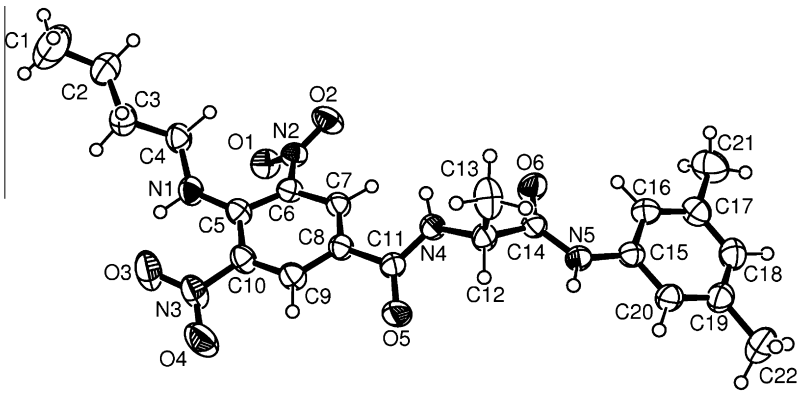

Fig. 2. ORTEP drawing of the *R*-enantiomer of ***rac*-I**. Displacement ellipsoids are drawn at the 50% probability level.

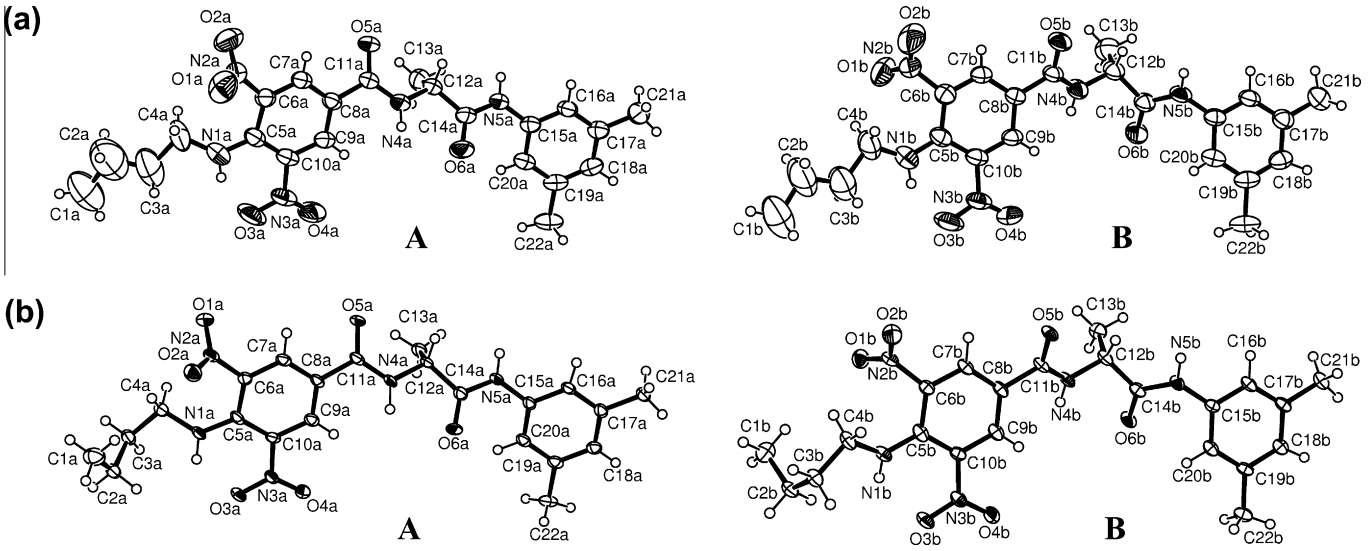

Fig. 3. Two conformers, **A** and **B** of ***R*-I** at: (a) room temperature, (b) at 100 K. Displacement ellipsoids are drawn at the 50% probability level.

Table 2
Selected torsion angles of heterochiral (***rac*-I**, *R*-configuration) and homochiral (***R*-I**) structures.

	***rac*-I**	***R*-I**, **A** (RT)	***R*-I**, **B** (RT)	***R*-I**, **A** (100 K)	***R*-I**, **B** (100 K)
C1–C2–C3–C4	−176.5(4)	174.5(12)	−178.4(12)	58.7(5)	−57.9(5)
C2–C3–C4–N1	−173.1(3)	178.4(12)	−179.8(11)	67.3(5)	−65.7(5)
C3–C4–N1–C5	−145.3(3)	159.7(7)	−172.3(6)	163.6(4)	−169.5(4)
C4–N1–C5–C6	−16.0(4)	17.0(9)	−11.8(7)	27.8(7)	−22.5(7)
C7–C8–C11–N4	25.1(4)	161.7(3)	−151.1(4)	164.9(4)	−153.4(4)
C8–C11–N4–C12	173.9(2)	162.9(3)	179.4(4)	162.8(4)	−177.0(4)
C11–N4–C12–C13	−113.9(3)	−69.2(3)	−100.2(5)	−68.4(5)	−98.3(5)
C11–N4–C12–C14	125.9(2)	171.0(3)	139.5(4)	171.7(4)	142.5(4)
N4–C12–C14–N5	−146.4(2)	−170.3(3)	−136.6(4)	−174.4(4)	−136.6(4)
C12–C14–N5–C15	−172.9(2)	−165.2(4)	−170.4(4)	−165.6(4)	−169.5(4)
C14–N5–C15–C16	5.4(4)	−149.8(4)	138.6(4)	−150.5(4)	138.3(4)

See Fig. 2. for atom labeling.

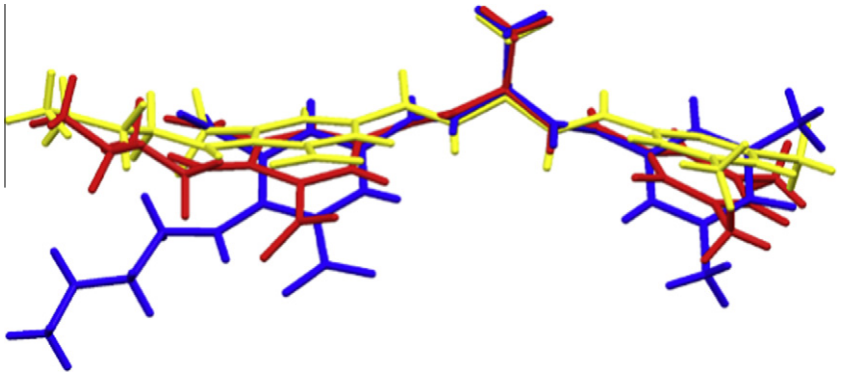

Fig. 4. Overlap of **A** (yellow) and **B** (blue) molecules in ***R*-I** at room temperature and *R*-enantiomer (red) selected from heterochiral (racemic) crystal. The overlap is made by least-squares fit of atoms forming the central part of the molecule (N4, O5, C12, C13, C14, O6, N5; see Fig. 2 for atom labeling).

A and **B** molecules) from planarity about ±30°. Overlap of **A** and **B** molecules of ***R*-I** at room temperature and *R*-enantiomer of heterochiral crystal, visualizes their conformational diversities (Fig. 4).

3.2. Crystal packing

In ***rac*-I** (Fig. 5, Table 3) molecules of opposite chirality (*RS* pairs) are linked by a pair of inversion symmetry-related N4–H4N···O6 hydrogen bonds generating dimeric rings of $R_2^2(10)$. The other amide group is proton donor to nitro group in hydrogen bond N5–H5N···O1 that links the homochiral molecules (*S*–*S*, *R*–*R*) into chain $C_2^2(11)$ extending in the direction [0 1 0]. The amino group N1–H acts as a donor to oxygen atom of the nitro group in intramolecular hydrogen bond (*S*6). The hydrogen bonds C–H···O, formed with strong acceptors such as amide oxygen and nitro group oxygen atoms, contribute to the linkage of these chains into double layers parallel to the direction [0 0 1].

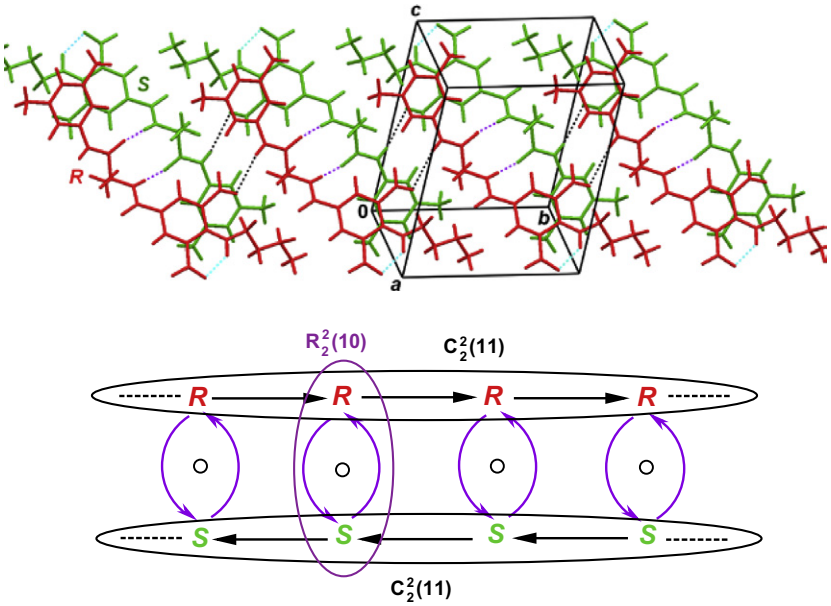

Fig. 5. Crystal packing of ***rac*-I** with differently colored *R* (red) and *S* (green) enantiomers. Hydrogen bonds N–H···O generate: heterochiral dimeric rings $R_2^2(10)$ (violet dashed lines), homochiral chains $C_2^2(11)$ (black lines) and the homochiral $S(6)$ (turquoise lines in packing diagram). Topology of hydrogen bonding network is schematically presented.

Table 3
Geometric parameters of hydrogen bonds present in the ***rac*-I** and ***R*-I** crystals.

Structure	Hydrogen bond	*D*–H (Å)	H···*A* (Å)	*D*–H···*A* (Å)	*D*–H···*A* (°)	Symm. operation on *A*
rac-I (RT)	N4–H4 N···O6	0.86(3)	2.09(3)	2.931(3)	163(3)	$1-x, 1-y, 1-z$
	N5–H5 N···O1	0.83(3)	2.63(3)	3.269(3)	166(2)	$-x, 1-y, 1-z$
	N1–H1 N···O3	0.96(3)	1.89(3)	2.649(3)	135(3)	x, y, z
	C12–H12···O1	0.98(3)	2.59(3)	3.442(3)	146(3)	$x, -1+y, z$
	C7–H7···O6	0.99(3)	2.82(3)	3.345(4)	114(2)	$1-x,1-y,1-z$
	C13–H13B···O2	0.98(4)	2.59(4)	3.379(4)	138(3)	$1-x, 1-y, 1-z$
	C20–H20···O5	1.02(3)	2.51(3)	3.497(3)	164(3)	$2-x, -y, 1-z$
	C22–H22A···O4	0.90(6)	2.69(5)	3.441(5)	141(5)	$2-x, -y, 1-z$
R-I (100 K)	N4A–H4A···O6B	0.93(9)	2.12(9)	3.031(5)	164(7)	$1+x, -1+y, z$
	N4B–H4B···O6A	0.86	2.21	3.008(5)	155	$-1+x, 1+y, z$
	N5A–H5A···O5B	0.86	2.19	3.025(5)	165	x, y, z
	N5B–H5B···O5A	0.87(9)	2.12(9)	2.978(5)	170(7)	x, y, z
	N1A–H1A···O4A	0.86	2.08	2.637(5)	121	x, y, z
	N1B–H1B···O3B	0.86	2.03	2.626(5)	125	x, y, z
	C9A–H9A···O6B	0.93	2.50	3.081(5)	121	$1+x, -1+y, z$
	C9B–H9B···O6A	0.93	2.89	3.514(8)	125	$-1+x,1+y, z$
	C12A–H12A···O5B	0.98	2.67	3.291(5)	122	x, y, z
	C13A–H13B···O5B	0.96	2.70	3.373(5)	128	x, y, z
	C21B–H21D···O1A	0.96	2.46	3.130(6)	127	x, y, z
	C22B–H22D···O5A	0.96	2.46	3.408(5)	168	$x, 1+y, z$
R-I (RT)	N4A–H4A···O6B	0.86	2.23	3.078(5)	167	$1+x, -1+y, z$
	N4B–H4F···O6A	0.86	2.25	3.062(6)	158	$-1+x, 1+y, z$
	N5A–H5A···O5B	0.86	2.16	3.004(4)	167	x, y, z
	N5B–H5B···O5A	0.86	2.16	2.994(6)	165	x, y, z
	N1A–H1G···O3A	0.87(3)	1.86(4)	2.606(6)	142(5)	x, y, z
	N1B–H1H···O3B	1.13(6)	1.63(6)	2.604(6)	141(6)	x, y, z
	C9A–H9A···O6B	0.92(4)	2.56(5)	3.098(5)	118(4)	$1+x, -1+y, z$
	C9B–H9B···O6A	0.82	2.94(8)	3.443(5)	117(6)	$-1+x, 1+y, z$
	C12A–H12A···O5B	0.97(4)	2.67(4)	3.330(5)	126(3)	x, y, z
	C18B–H18B···O1A	1.09(6)	2.72(7)	3.397(7)	120(4)	$-1+x, 1+y, z$
	C22B–H22F···O1A	0.96	2.67	3.470(7)	141	$-1+x, 1+y, z$
	C22A–H22C···O3B	0.96	2.71	3.445(7)	134	$1+x, -1+y, z$
	C21B–H21F···O2A	0.96	2.54	3.223(9)	129	x, y, z

The crystal packing of ***R*-I** at both temperatures reveals the same topology of hydrogen bond network but completely different comparing to ***rac*-I** (Fig. 6, Table 3). In *R*-**I** crystal the molecule **A** vs. **B** is rotated for about 180° to avoid steric hindrance between C13-methyl groups attached to the stereogenic C12 atoms (of both conformers) and to make approachable both amide groups for hydrogen bonding between two neighboring conformers (**A**, **B**). Two amide groups of each of the conformers acting as donors

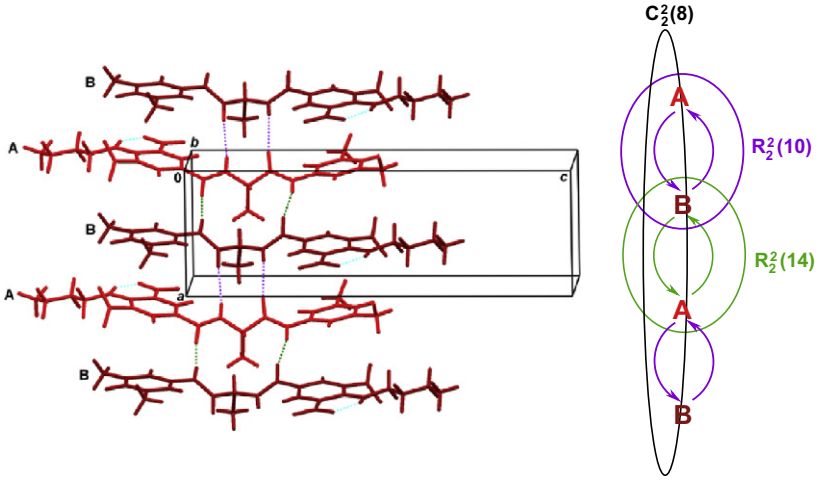

Fig. 6. Crystal packing of ***R*-I** with two molecules in the asymmetric unit: **A** (light-red) and **B** (dark-red). Intermolecular N–H···O hydrogen bonds between the conformers **A** and **B** generate R_2^2 (10) (violet dashed lines), R_2^2 (14) (green dashed lines), C_2^2 (8), and intramolecular S(6) bonds (turquoise).

Table 4
Temperatures of fusion (T_{fus}/K), enthalpies (kJ mol^{-1}) in italics and the dimensionless value of $\Delta S/R$ in square brackets, temperatures of glass transition (Tg/K) and corresponding specific heat (J mol^{-1} K^{-1}) in italics of heterochiral and homochiral selector.

Selector	T_{fus} (Cr$_s$)	T_{fus} (Cr$_m$)	Tg
rac-I	497		351
	63.03 [15.25]		0.27
R-I	453	471	351
	19.59 [5.20]	36.84 [9.4]	0.29
S-I	456	471	351
	21.74 [5.73]	38.21 [9.74]	0.24

Cr$_s$, crystals obtained from the solution; Cr$_m$, crystals obtained from the melt.

and acceptors in the hydrogen bonds N–H···O generate the ring motif $R_2^2(10)$ and $R_2^2(14)$ that are interlinked by a chain $C_2^2(8)$ along the direction [0 1 0]. Analogous to ***rac*-I** the amino group N1–H in both conformers of ***R*-I** act as a donor to oxygen atom of the nitro group establishing an intramolecular hydrogen bond.

3.3. Thermal behavior

The differences in the crystal packing of the heterochiral and homochiral selectors are reflected in the variations of the thermal behavior summarized in Table 4. While ***rac*-I** simply melted at 497 K enantiomers ***R*-I** and ***S*-I** displayed two melting points that correspond to the melting of two crystal forms.

Polarizing optical microscopy investigation of homochiral selectors revealed the presence of two crystal forms. Upon heating as the plate-like crystals obtained from the solution (denoted as Cr$_s$) melt while the needle-like crystals (denoted as Cr$_m$) grow (Fig. 7) and then melt at higher temperature. On cooling neither heterochiral nor homochiral selector recrystallize from the melt, instead formation of an amorphous solid was observed.

The thermal behavior was confirmed and quantified by calorimetric measurements. The DSC trace of the first heating run (2 K/min) for ***R*-I** (Fig. 8a) shows that melting of Cr$_s$ at 453 K is followed by immediate crystallization of Cr$_m$ at 455 K and final melting at 571 K. In addition, the Cr$_m$ form has the enthalpy (ΔH_{fus} = 36.84 kJ mol^{-1}) and corresponding entropy of fusion ($\Delta S_{fus}/R$ = 9.40) almost twice higher than the Cr$_s$ form (ΔH_{fus} = 19.59 kJ mol^{-1}; $\Delta S_{fus}/R$ = 5.20) pointing to a substantial difference in thermodynamic stability and in "crystal ordering" between the two forms. In the cooling cycle (Fig. 8b) the observed low intensity exothermic transition (ΔCp = 0.29 J mol^{-1} K^{-1}) to an amorphous solid at 351 K was assigned to a glass transition. In the second heating run (10 K/min) this solid undergoes the glass transition

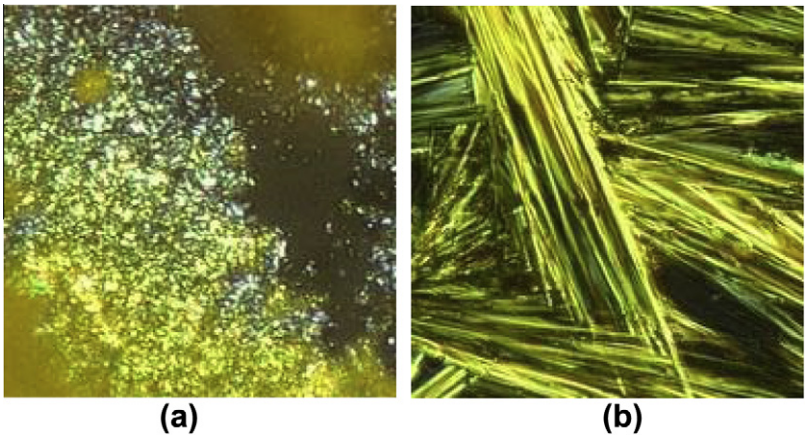

Fig. 7. Photomicrographs of *R*-**I** obtained in the first heating run: (a) plate-like crystals of the Cr$_s$ form at 423 K, (b) needle-like crystals of the Cr$_m$ form at 467 K (magnification 500×).

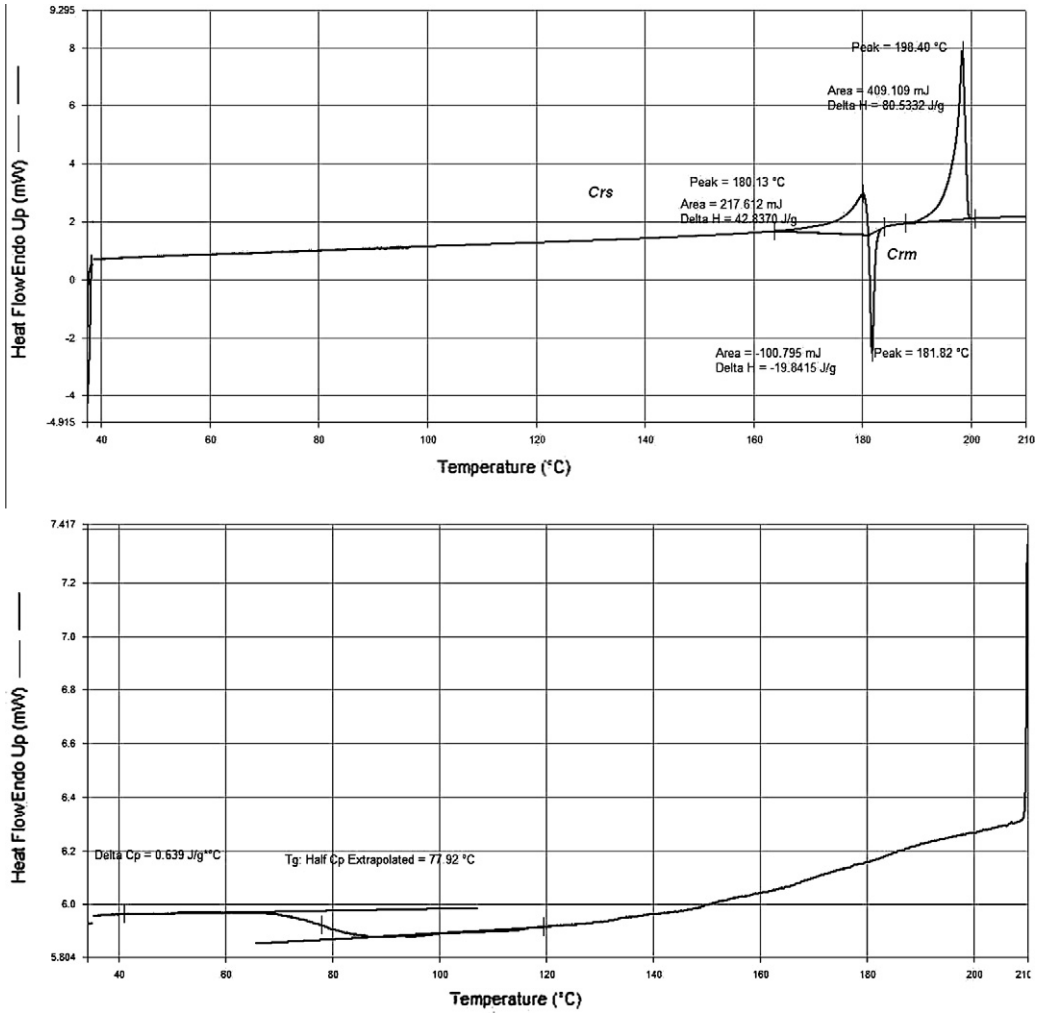

Fig. 8. DSC thermograms of ***R*-I** (a) the first heating run at rate 2 K/min and (b) the first cooling run at rate 10 K/min.

at 355 K followed by crystallization at 444 K (see ESI Fig. S1c). The newly formed crystal form melt at 470 K, approximate the same melting temperature observed for the Cr_m form in the first heating run. Absence of the endothermic signal at 456 K in the second heating cycle reveals that the structure of Cr_s is permanently transformed into Cr_m form under thermal stress. As expected, a similar behavior pattern was observed for the ***S*-I** enantiomer (see ESI, Figs. S2 and S3). However, although the melting points of Cr_m forms and Tg of both enantiomers are the same, surprisingly the temperatures of melting of the Cr_s form (456 K) and crystallization (457 K) of the Cr_m form of *S*-enantiomer are higher than those observed for the *R*-enantiomer. Despite of a small difference in the melting temperatures of two enantiomeric Cr_s forms, thermodynamic data associated with this process (Table 4) are roughly equal suggesting that the both enantiomeric Cr_s forms are of the same thermodynamic stability and the ''crystal ordering" as expected. Calorimetric studies performed on ***rac*-I** are in agreement with microscopy observation revealing single melting point at 497 K with enthalpy of fusion of $\Delta H_{fus} = 63.03$ kJ mol^{-1} and entropy parameter $\Delta S_{fus}/R$ of 15.25 and on cooling a glass transition at 351 K ($\Delta Cp = 0.27$ J mol^{-1} K^{-1}), (see ESI, Figs. S4 and S5).

The results presented above show that hydrogen bonding primary control the packing mode in the crystals. The packing of heterochiral crystal of ***rac*-I** is 3.5% denser than the homochiral crystal of ***R*-I** (1.355 g cm^{-3} vs. 1.309 g cm^{-3}) that reflected on its higher temperature of fusion and thermodynamic stability. In both crystals, heterochiral and homochiral, the intermolecular hydrogen bonding involving amide groups represents the building block of crystal packing. Presence of aminobutyl chain and dinitrophenyl group in the molecular structure allows additional hydrogen bonding. Thus in crystal of ***rac*-I** both nitro groups are engaged: intermolecular bonding between H of dimethylphenyl-amide group and oxygen of nitro group on neighboring molecule (H5N···O1′) links the homochiral molecules (*S*–*S*, *R*–*R*), and intramolecular bonding between H of aminobutyl group and oxygen atom of the nitro group occurs. In the homochiral crystal of ***R*-I** the nitro group is forming only intramolecular hydrogen bonding with the adjacent amino group giving to the rest of molecule higher degree of conformational freedom. Furthermore, the flexibility of *n*-butyl chain is associated with large thermal motions of these atoms that do not disappear at 100 K, leading to dynamical disorder. Thermo-optical investigation reveals that observed difference in crystal packing has a great impact on thermodynamic properties. Despite of flexibility of *n*-butyl chain, intermolecular hydrogen bonding that fix not only the middle alanine moiety but also the terminal dinitrophenyl group resulted in the high entropy of fusion ($\Delta S_{fus}/R = 15.25$) of ***rac*-I** pointing to good ''crystal ordering". On the contrary, the homochiral crystal Cr_s, where only amide groups form hydrogen bonding, is unstable under thermal stress and its entropy term $\Delta S_{fus}/R$ abate to 5.20 suggesting considerable reduced ''crystal ordering" most likely caused by conformational disorder within the crystal.

4. Conclusion

The structural studies of heterochiral ***rac*-I** and homochiral ***R*-I** using X-ray structure analysis were complemented thermo-optical analysis using differential scanning calorimetry and hot-stage polarizing optical microscopy. Crystal packing of these compounds is dominated by an intermolecular hydrogen bonding with different topologies and consequently they display different thermodynamic stability. The heterochiral crystal is characterized by high temperature and entropy of fusion as a result of compact packing of the molecules of opposite chirality (*RS* pairs) and good "crystal ordering". However packing of the molecules of the same chirality leads to the crystal of low thermodynamic stability implying rather high degree of conformational freedom.

Acknowledgements

The authors are indebted to Dr. Irina Pucić from Ruđer Bošković Institute for help and valuable suggestions concerning DSC measurements. This work was supported by Ministry of Science, Education and Sports of Croatia (Grant nos. 098-1191344-2943 and 098-0982904-2910).

Appendix A. Supplementary material

Supplementary data associated with this article can be found, in the online version, at doi:10.1016/j.molstruc.2010.06.036.

References

[1] C.O. Kappe, Tetrahedron 49 (1993) 6937.
[2] C.O. Kappe, Acc. Chem. Res. 33 (2000) 879.
[3] C.O. Kappe, Eur. J. Med. Chem. 35 (2000) 1043.
[4] T.A. Baillie, K.M. Schultz, Stereochemistry in drug development process: role of chirality as a determinant of drug action metabolism and toxicity, in: H.Y. Aboul-Enein, I.W. Wainer (Eds.), The Impact of Stereochemistry on Drug Development and Use, John Wiley & Sons Inc., 1997, pp. 21–45.
[5] D. Kontrec, V. Vinković, V. Šunjić, B. Schuiki, W.M.F. Fabian, C.O. Kappe, Chirality 15 (2003) 550.
[6] I. Gazić, D. Kontrec, A. Lesac, V. Vinković, Tetrahedron: Asymmetry 16 (2005) 1182.
[7] D. Moslavac Forjan, M. Vinković, D. Kontrec, A. Lesac, V. Vinković, Struct. Chem. 18 (2007) 585.
[8] K. Harms, S. Wocadlo, XCAD-4 Program for Processing CAD4 Diffractometer Data, University of Marburg, Germany, 1995.
[9] A.C.T. North, D.C. Philips, F.S. Mathews, Acta Cryst. A 24 (1968) 351.
[10] L.J. Farrugia, J. Appl. Cryst. 32 (1999) 837.
[11] G.M. Sheldrick, Acta Crystallogr. A 64 (2008) 112.
[12] T. Spek, PLATON98: A Multipurpose Crystallographic Tool, 120398 Version, University of Utrecht, Utrecht, The Netherlands, 1998.
[13] L.J. Farrugia, J. Appl. Cryst. 30 (1997) 565.
[14] I.J. Bruno, J.C. Cole, P.R. Edgington, M.K. Kessler, C.F. Macrae, P. McCabe, J. Pearson, R. Taylor, Acta Crystallogr. B 58 (2002) 389.
[15] I.K. Reddy, R. Mehvar (Eds.), Chirality in Drug Design and Development, Marcel Dekker, New York, 2004.
[16] R.J. Kazlauskas, A.N.E. Weissfloch, A.T. Rappaport, L.A. Cuccia, J. Org. Chem. 56 (1991) 656.
[17] C. Brock, W.B. Schweizer, J.D. Dunitz, J. Am. Chem. Soc. 113 (1991) 9811.
[18] O. Wallach, Liebigs Ann. Chem. 286 (1895) 90.
[19] K. Marthi, S. Larsen, M. Ács, E. Fogassy, J. Mol. Struct. 374 (1996) 347.
[20] B.O. Patrick, C.P. Brock, Acta Cryst. B62 (2006) 488.
[21] V.J. Blazis, K.J. Koeller, N.P. Rath, Ch.D. Spilling, Acta Cryst. B53 (1997) 838.
[22] W. Klyne, V. Prelog, Experientia 16 (1960) 521.